

Subsequent Boundary Distance Regression and Pixelwise Classification Networks for Automatic Kidney Segmentation in Ultrasound Images

Shi Yin, Qinmu Peng, Hongming Li, Zhengqiang Zhang, Xinge You, *Senior Member, IEEE*, Susan L. Furth, Gregory E. Tasian, Yong Fan, *Senior Member, IEEE*

Abstract—It remains challenging to automatically segment kidneys in clinical ultrasound (US) images due to the kidneys' varied shapes and image intensity distributions, although semi-automatic methods have achieved promising performance. In this study, we propose subsequent boundary distance regression and pixel classification networks to segment the kidneys, informed by the fact that the kidney boundaries have relatively homogenous texture patterns across images. Particularly, we first use deep neural networks pre-trained for classification of natural images to extract high-level image features from US images, then these features are used as input to learn kidney boundary distance maps using a boundary distance regression network, and finally the predicted boundary distance maps are classified as kidney pixels or non-kidney pixels using a pixel classification network in an end-to-end learning fashion. We also proposed a novel data-augmentation method based on kidney shape registration to generate enriched training data from a small number of US images with manually segmented kidney labels. Experimental results have demonstrated that our method could effectively improve the performance of automatic kidney segmentation, significantly better than deep learning based pixel classification networks.

Index Terms—Ultrasound images, fully automatic segmentation, deep neural networks, boundary detection, boundary distance regression, pixelwise classification

I. INTRODUCTION

ULTRASOUND (US) imaging has been widely used to aid diagnosis and prognosis of acute and chronic kidney

diseases [1, 2]. In particular, anatomic characteristics derived from US imaging, such as renal elasticity, are associated with kidney function [3, 4] and lower renal parenchymal area as measured on US imaging data is associated with increased risk of end-stage renal disease (ESRD) in boys with posterior urethral valves [2]. Imaging features computed from US data using deep convolutional neural networks (CNNs) improved the classification of children with congenital abnormalities of the kidney and urinary tract (CAKUT) and controls [5, 6]. The computation of these anatomic measures typically involves manual or semi-automatic segmentation of kidneys in US images, which increases inter-operator variability and reduces reliability. Therefore, automatic and reliable segmentation of the kidney from US imaging data is desired.

Since manual segmentation of the kidney is time consuming, labor-intensive, and highly prone to intra- and inter-operator variability, semi-automatic and interactive segmentation methods have been developed [7]. Particularly, an interactive tool has been developed for detecting and segmenting the kidney in 3D US images [8]. A semi-automatic segmentation framework based on both texture and shape priors has been proposed for segmenting the kidney from noisy US images [9]. A novel graph-cuts method has been proposed to segment the kidney in US images by integrating image intensity information and texture feature maps [10]. A variety of methods have been proposed to segment the kidney based on active shape models and statistical shape models [8, 11-14]. Random forests have also been adopted in a semi-automatic segmentation method to

This paper was submitted on November 11, 2018. This work has been submitted to the IEEE for possible publication. Copyright may be transferred without notice, after which this version may no longer be accessible.

Shi Yin is with the School of Electronic Information and Communications, Huazhong University of Science and Technology, Wuhan, China and the Department of Radiology, Perelman School of Medicine, University of Pennsylvania, Philadelphia, PA, 19104, USA and (e-mail: m201371756@hust.edu.cn).

Qinmu Peng, Zhengqiang Zhang, Xinge You are with the School of Electronic Information and Communications, Huazhong University of Science and Technology, Wuhan, China (e-mails: pengqinmu@hust.edu.cn; xtudbxk@hust.edu.cn; youxg@hust.edu.cn).

Hongming Li and Yong Fan are with the Department of Radiology, Perelman School of Medicine, University of Pennsylvania, Philadelphia, PA, 19104, USA (e-mails: Hongming.Li@uphs.upenn.edu; Yong.Fan@IEEE.ORG; Yong.Fan@uphs.upenn.edu).

Susan L. Furth is with the Department of Pediatrics, Division of Pediatric Nephrology, The Children's Hospital of Philadelphia, Philadelphia, PA 19104, USA (e-mail: FurthS@email.chop.edu).

Gregory E. Tasian is with the Department of Surgery, Division of Pediatric Urology, The Children's Hospital of Philadelphia, Philadelphia, PA 19104, USA; the Center for Pediatric Clinical Effectiveness, The Children's Hospital of Philadelphia, Philadelphia, PA 19104, USA, and the Department of Biostatistics, Epidemiology, and Informatics, The University of Pennsylvania, Philadelphia, PA, 19104, USA (e-mail: TasianG@email.chop.edu).

segment the kidney [15]. Although a variety of strategies have been adopted in the semi-automatic kidney segmentation methods, most of them solve the kidney segmentation problem as a boundary detection problem and rely on manual operations for initializing the semi-automatic segmentation.

Deep convolutional neural networks (CNNs) have demonstrated excellent performance in a variety of image segmentation problems, including semantic segmentation of natural images [16, 17] and medical image segmentation [18-20]. Recently, several methods have been proposed to automatically segment the kidney from medical imaging data to generate kidney masks using deep CNNs. In particular, U-net networks have been adopted to segment the kidney by classifying image pixels/voxels as kidney or non-kidney ones in a pattern classification based setting [21-24]. In these pattern classification based kidney segmentation methods, all pixels/voxels within the kidney have the same kidney classification labels, ignoring large variability of the kidneys in both appearance and shape in US images. As shown in Fig. 1, kidneys may have varied shapes and heterogeneous appearances in US images. Such shape and appearance variability, in conjunction with inherent speckle noise of US images, may degrade performance of the pixelwise pattern classification based kidney segmentation methods [25].

On the other hand, several recent studies have demonstrated that pixelwise pattern classification based image segmentation methods could achieve improved image segmentation performance by incorporating boundary detection as an auxiliary task in both natural image segmentation [26, 27] and medical image segmentation [28-30]. However, the performance of these methods is hinged on their image pixelwise classification component as the boundary detection serves as an auxiliary task for refining edges of the pixelwise segmentation results.

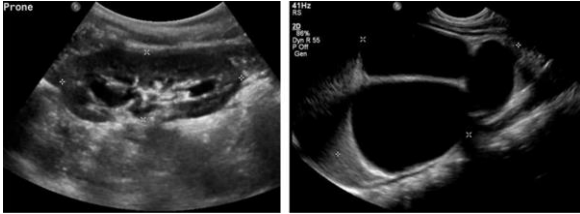


Fig. 1. Kidneys in US images may have varied shapes and the kidney pixels typically have heterogeneous intensities and textures.

Inspired by the excellent performance of the semi-automatic boundary detection based kidney segmentation methods, we develop a fully automatic, end-to-end deep learning method to subsequently learn kidney boundaries and pixelwise kidney masks from a set of manually labeled US images. Instead of distinguishing kidney pixels from non-kidney ones in a pattern classification setting, we learn CNNs in a regression setting to detect kidney boundaries that are modeled as boundary distance maps. From the learned boundary distance maps, we learn pixelwise kidney masks by optimizing their overlap with the manual kidney segmentation labels. To augment the training dataset, we adopt a kidney shape based image registration

method to generate more training samples. Our deep CNNs are built upon an image segmentation network architecture derived from DeepLab [17] so that existing image classification/segmentation models could be reused as a starting point of the kidney image segmentation in a transfer learning framework to speed up the model training and improve the performance of the kidney image segmentation. We have evaluated the proposed method for segmenting the kidney based on clinical US images, including 100 US images of normal kidneys and 85 US images of abnormal kidneys. The evaluation results have demonstrated that the proposed method could achieve promising segmentation performance and outperformed alternative state-of-the-art deep learning based image segmentation methods.

II. METHODS AND MATERIALS

A. Imaging Data

All the imaging data used in this study were collected using standard clinical US scanners at the Children's Hospital of Philadelphia (CHOP). The dataset contains the first post-natal US images of kidneys from 50 children with congenital abnormalities of the kidney and urinary tract (CAKUT) and the first post-natal US images of the kidneys of 50 children with unilateral mild hydronephrosis (Society of Fetal Urology grade I-II). Mild hydronephrosis is generally a benign finding that does not affect the appearance of the affected or contralateral normal kidney [31-33]. From these subjects, in total 185 US images were obtained, including 100 normal scans and 85 abnormal scans. The images were manually segmented by experts from the CHOP. Representative normal and abnormal kidney US images are shown in Fig.1. These images were resized to have a size of 321×321 , and their image intensities were linearly scaled to $[0, 255]$. We randomly selected 105 images as training data, 20 images as validation data, and 60 images as testing data to evaluate kidney segmentation methods.

B. Deep CNN Networks for Kidney Image Segmentation

The kidney image segmentation method is built upon deep CNNs to subsequently detect kidney boundaries and kidney masks in an end-to-end learning fashion. As illustrated in Fig.2, the kidney image segmentation model consists of a transfer learning network, a boundary distance regression network, and a kidney pixel classification network. The transfer learning network is built upon a general image classification network to reuse an image classification model as a starting point for learning high level image features from US images, the boundary distance regression network learns kidney boundaries modeled as distance maps of the kidney boundaries, and the kidney boundary distance maps are finally used as input to the kidney mask learning network to generate kidney segmentation masks. The kidney boundary detection network and the kidney mask learning network are trained based on augmented training data that are generated using a kidney shape based image registration method. The network architecture and the data augmentation methods are described in following sections.

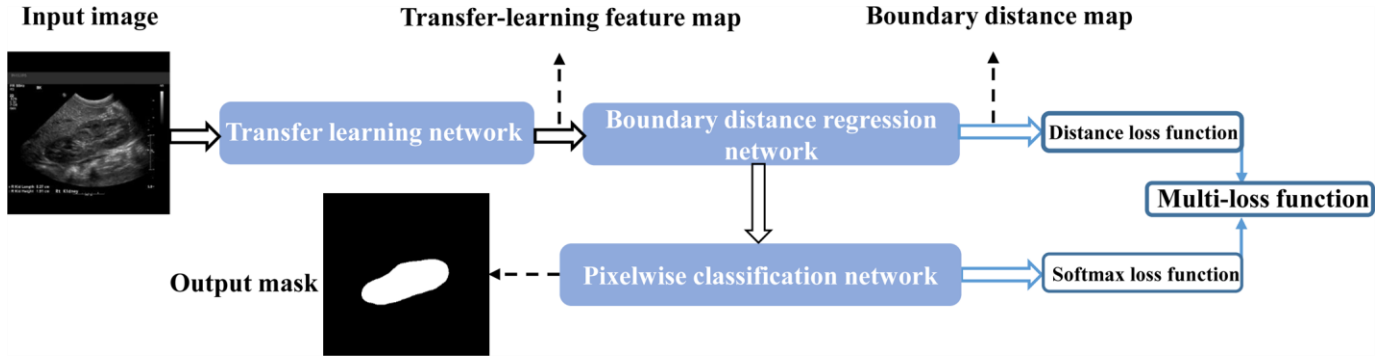


Fig. 2. Transfer learning network, and subsequent boundary distance regression and pixel classification networks for fully automatic kidney segmentation in US images.

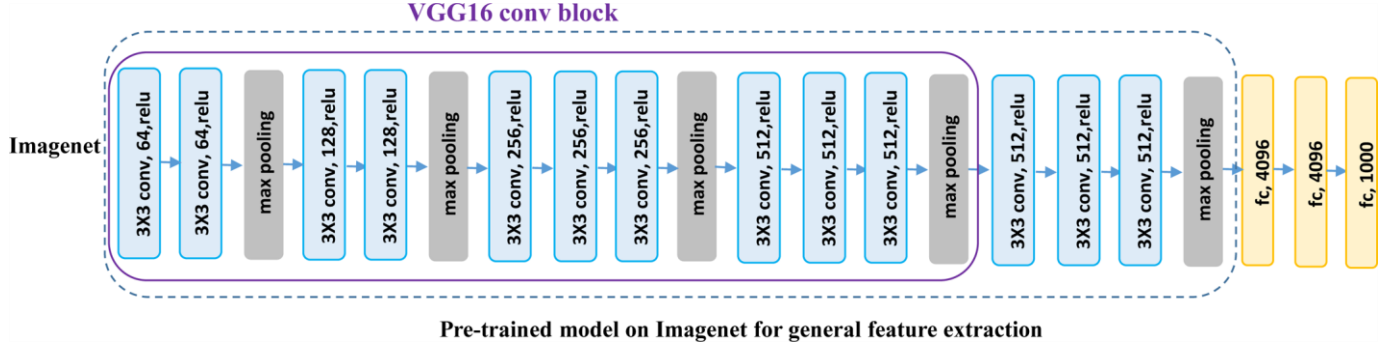


Fig. 3. The architecture of the VGG16 model.

1) Transfer learning network for extracting high level image features from US images

Instead of directly building an image segmentation network on raw US images, we adopt a transfer learning strategy to extract informative image features from US images as a starting point for learning high level image features from US images. Particularly, we extract features from US images by utilizing a general image classification network, namely VGG16, which achieves 92.7% top-5 test-accuracy in ImageNet [34].

As illustrated in Fig. 3, the VGG16 network consists of 16 convolutional (conv) layers with a receptive field of 3×3 . The stack of convolutional layers is followed by 3 fully-connected (FC) layers: each of the first two has 4096 channels and the third performs 1000-way classification. The final layer is a softmax layer. In our experiments, we fine-tuned the model weights of Imagenet-pretrained VGG16 network to adapt them to the boundary distance regression network.

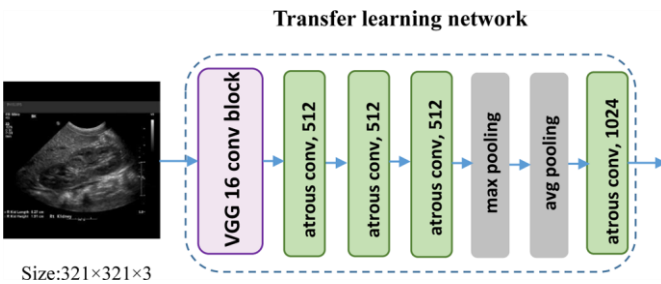


Fig. 4. The architecture of the Deeplab model. We extracted the pretrained feature maps L from the exiting Deeplab model.

On the other hand, we follow the Deeplab architecture [17]

by applying the atrous convolutions to compute denser image feature representations. As illustrated in Fig. 4, the Deeplab image segmentation model modified the last 3 convolutional layers and FC layers into 4 atrous convolutional layers and 2 convolutional classification layers. We discarded the 2 convolutional classification layers to adapt the architecture to the boundary distance regression network.

2) Boundary distance regression network for fully automatic kidney segmentation in ultrasound images

We develop a boundary distance regression network for fully automatic kidney segmentation in ultrasound images, instead of learning a pixelwise classification network directly from the US image features because the heterogenous kidney appearances in US images make it difficult to directly classify pixels as kidney or background pixels.

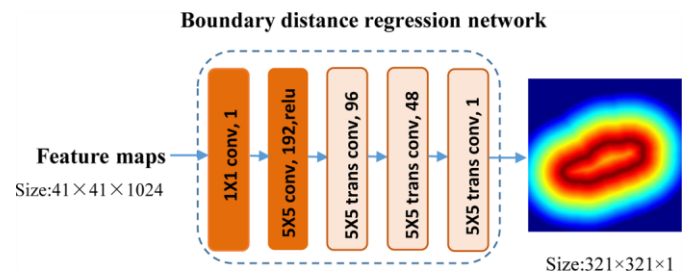


Fig. 5. Network architecture of the boundary distance regression network.

The boundary distance regression network is built in a regression framework, consisting of two parts: a projection part that produces boundary feature maps S_0 and a high-resolution

reconstruction part that upsamples the feature maps to obtain the kidney distance maps at the same spatial resolution of the input images as illustrated in Fig. 5. The projection part is built on two convolutional layers, and the reconstruction part is built on deconvolution (transposed convolution) layers. The output of the i th deconvolution operation S_i is defined as

$$S_i = \max(0, W_i \otimes S_{i-1} + B_i), \quad (1)$$

where W_i is deconvolution filters with size $f_i \times f_i$, and B_i is a bias vector, and \otimes is deconvolution operator. The upsampling deconvolution layers increase the spatial dimension of their input feature maps by 2 folds, and therefore 3 upsampling deconvolution layers are adopted in the kidney boundary distance regression network to learn the kidney boundary in the input image space. In our experiments, the numbers of input feature maps of the upsampling deconvolution layers were empirically set to 3 times of 64, 32, 16 respectively, and the filter size f_i was empirically set to 5.

We solve the kidney boundary detection problem in a regression framework to learn distance from the kidney boundary at every pixel of the input US images. The kidney boundary detection problem could be potentially solved in an end-to-end classification framework [35]. However, the number of the kidney boundary pixels is much smaller than the number of non-boundary pixels in US kidney images. Such unbalanced boundary and non-boundary pixels make it difficult to learn an accuracy classification model. Therefore, we model the kidney boundary detection as a distance map learning problem.

Given an input US image I with its kidney boundary, we compute the distance to the kidney boundary for every pixel $P_i \in I$ of the input image and obtain a normalized kidney distance map of the same size of the input image using potential function as following:

$$d(P_i) = \exp(-\lambda D_i), \quad (2)$$

with $D_i = \min_{b_j \in \mathbf{b}} \text{dist}(P_i, b_j)$ is the minimal Euclidean distance of pixel P_i to the kidney boundary pixels $\mathbf{b} = \{b_j\}_{j \in J}$, and λ is a parameter. As illustrated in Fig.6, at the kidney boundary pixels the normalized exponential kidney distance equals to 1. In this study, the kidney boundary is detected by learning the normalized kidney distance map.

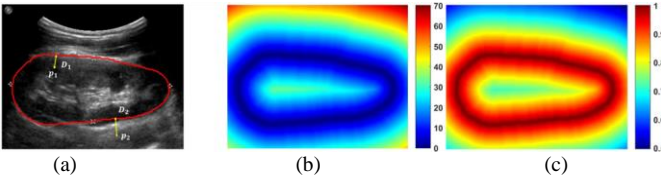


Fig. 6. An example kidney US image and kidney boundary (a), its boundary distance map (b), and its normalized potential distance map with $\lambda = 1$ (c). The colorbar of (c) is in log scale.

To learn the normalized kidney boundary distance map, we train the boundary detection network by minimizing a distance loss function L_d , defined as,

$$L_d = \sum_{P_i \in I} \|\varphi(P_i) - d(P_i)\|^2, \quad (3)$$

where $\varphi(P_i)$ is the predicted distance and $d(P_i)$ is the ground truth distance to the kidney boundary at pixel P_i . Once we

obtain the predicted distance for every pixel of a US image to be segmented, we can obtain a boundary binary map with a threshold $e^{-\lambda}$.

To obtain a smooth closed contour of the kidney boundary, we construct a minimum spanning tree of all predicted kidney boundary pixels. Particularly, we first construct an undirected graph of all predicted kidney boundary pixels, each pair of which are connected with a weight of their Euclidean distance. Then, a minimum spanning tree T is obtained using Kruskal's algorithm [36]. Finally, the max path of the minimum spanning tree T is obtained as a close contour of the kidney boundary and a binary mask of the kidney is subsequently obtained. To reduce the complexity of finding a minimum spanning tree, we could apply morphological operations to the binary kidney boundary image to obtain a skeleton binary map and apply the minimum spanning tree algorithm to the skeleton binary map. We refer to the boundary distance regression network followed by post-processing for segmenting kidneys as a boundary detection network hereafter.

3) Subsequent boundary distance regression and pixelwise classification networks for fully automatic kidney segmentation in ultrasound images

The minimum spanning tree post-processing method could obtain promising boundary detection results for most US kidney images. However, it fails if the predicted boundary distance maps are far from perfect. To obtain robust kidney segmentation performance, we propose to learn pixelwise kidney masks from the predicted kidney distance maps.

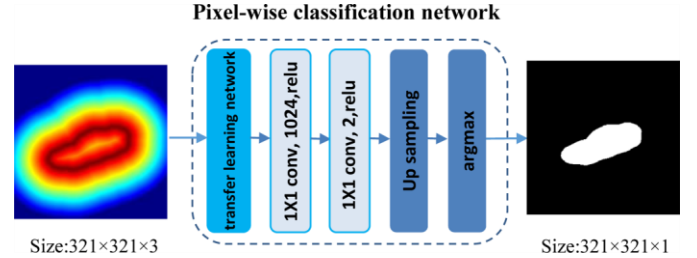


Fig. 7. Architecture of the kidney pixel classification network.

As illustrated in Fig. 7, the kidney pixelwise classification network is built upon a semantic image segmentation network, namely Deeplab image segmentation network. The input to the kidney pixel classification network is an image with 3 channels, each being the output of the predicted kidney boundary map. The final decision for class labels is then made by applying 2-channel classification softmax layer to the extracted class feature maps $f_{(c,P_i)}$ ($c=0,1$) based on cross-entropy loss function:

$$L_s = - \sum_{P_i \in I} \log \left[\frac{\exp(f_{(1,P_i)})}{\sum_{c=0}^1 \exp(f_{(c,P_i)})} \right]. \quad (4)$$

We also adopt the pre-trained VGG16 model to initialize the pixelwise classification network parameters.

To train the kidney boundary distance regression and pixelwise classification networks in an end-to-end fashion, loss functions of the kidney boundary distance regression network and the kidney pixelwise classification network are combined

with a multi-loss function

$$L_m = \left(1 - \frac{\tau}{N}\right)L_d + \frac{\tau}{N}\gamma L_s, \quad (5)$$

where N is the number of total iterative training steps, τ is an index of the training iteration step, and γ is a parameter to make L_d and L_s to have the same magnitude and to be determined empirically. The multi-loss function puts more weight on the kidney boundary distance regression cost function in the early stage of the network training and then shifts to the kidney pixel classification cost function in the late stage of the network training. The kidney pixelwise classification network's output is treated as the overall segmentation result.

C. Data augmentation based on kidney shape registration

To build a robust kidney segmentation model, we augment the training data using a non-rigid image registration method [37]. Particularly, in order to generate training US kidney images with varied kidney shapes and appearances, we register each training image to all other training images based on thin-plate splines transformation (TPS) [37] as following.

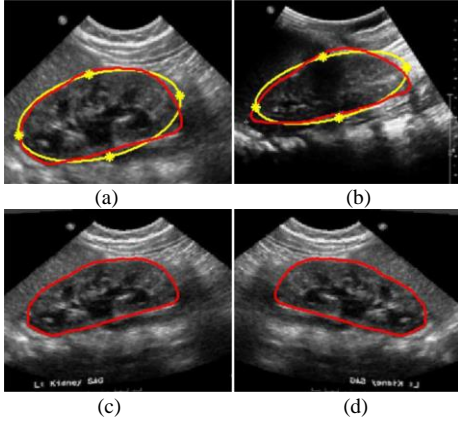


Fig. 8. Data-augmentation based on TPS transformation and flipping. (a) is a moving image, (b) is a fixed image, (c) is the registered image and (d) is the flipped registered image. The kidney shape denoted by the red curve is approximately modeled as an ellipse denoted by the yellow curves. The yellow stars denote the landmark points of the TPS transformation.

Given two US kidney images with kidney boundaries, we register one image (moving image M) to the other image (fixed image F), in order to generate a deformed moving image in the fixed image space. First, the kidney boundary is approximately modeled as an ellipse as shown in Fig. 8. Then, ellipse vertexes of the kidney are identified as 4 corresponding landmark points across kidneys, and the landmark points of the fixed and moving images are denoted by $Z_M = [x_M \ y_M]^T \in R^{2 \times 4}$ and $Z_F = [x_F \ y_F]^T \in R^{2 \times 4}$ respectively. Based on the corresponding landmark points, a TPS operation W is computed to register the moving image M to the fixed image F , defined as:

$$W = \begin{bmatrix} R & P^T \\ P & 0^{3 \times 3} \end{bmatrix}^{-1} \begin{bmatrix} Z_M^T \\ 0^{3 \times 2} \end{bmatrix}, \quad (6)$$

where $P = [I^{4 \times 1} \ Z_M^T]^T \in R^{3 \times 4}$ is the homogeneous coordinates of Z_M , and R is a symmetric matrix with elements $r_{i,j} = \phi(k(Z_M - Z_M k_2))$. Based on the estimated TPS transformation, a warped moving image could be generated. We use a nearest neighbor interpolation method to warp the

moving image. In addition to the image registration based data augmentation, we also flip the training images left to right. Given n training images, we can obtain $2n(n-1) + n$ augmented training images with kidney boundaries.

D. Implementation and Evaluation of the proposed method

The proposed networks were implemented based on Python 3.7.0 and Tensorflow r1.11. We used a mini-batch of 20 images to train the deep neural networks. The maximum number of iteration steps was set to 20000. The deep learning models were trained on a GeForce GTX 6.0GB graphics processing unit (GPU). The deep networks were optimized using Adam stochastic optimization [38] with the learning rate of 10^{-4} . Besides the parameters of transfer learning network, the filters of the boundary regression network were initialized with random normal initializer with the mean 0 and standard deviation 0.001. The biases of the boundary regression network were initialized with constant 0. In the subsequent kidney boundary detection and pixel classification network, γ was empirically set to 1 to make the kidney boundary regression and pixel classification loss functions to have similar magnitudes. The minimum spanning tree algorithm were implemented based on Networkx python library (<https://networkx.github.io/documentation/networkx-1.10/overview.html>).

Ablation studies were carried out to evaluate how different components of the proposed method affect the segmentation performance. We first trained the kidney boundary detection network using following 3 different strategies, including training from scratch without data augmentation (named “random+noaug”), transfer learning without data augmentation (named “finetune+noaug”), and transfer-learning with data augmentation (named “finetune+aug”). Particularly, for the training from scratch we adopted “Xavier” initialization method that has been widely adopted in natural image classification and segmentation studies [39]. Particularly, we initialized the biases to be 0 and filters to follow a uniform distribution. The training images’ normalized kidney boundary distance maps were obtained with $\lambda = 1$. Outputs of the kidney boundary detection network were post-processed using morphological operations and minimum spanning tree algorithm in order to obtain kidney masks.

Second, we trained and compared kidney boundary detection networks based on augmented training data and transfer-learning initialization with their normalized kidney distance maps obtained with different values of λ , including 0.01, 0.1, 1, and 10. We also trained a kidney boundary detection network in a classification setting. Particularly, the classification based kidney boundary detection network had the same network architecture as the regression based kidney boundary detection network, except that its loss function was a softmax cross-entropy loss to directly predict the kidney boundary pixels. Outputs of the kidney boundary detection network were also post-processed using the morphological operations and minimum spanning tree algorithm in order to obtain kidney masks.

Third, we trained and compared kidney boundary detection

networks with 2 state-of-the-art pixel classification based image segmentation deep neural networks, namely FCNN [16] and Deeplab [17]. The FCNN network and Deeplab compared in our paper were also adopted from the VGG16, the same one as adopted in our method. The comparisons were based on both the training data without augmentation and the augmented training data. Segmentation performance of all the methods under comparison was measured using Dice index, mean distance (MD), Jaccard, Precision, Sensitivity, ASSD defined in [40, 41]. The segmentation performance measures of testing images obtained by different segmentation networks were statistically compared using Wilcoxon signed-rank tests [42].

We also compared the proposed subsequent boundary distance regression and pixelwise classification networks with the kidney boundary detection network. We trained the subsequent boundary distance regression and pixelwise classification networks based on the augmented training data and transfer-learning initialization. Finally, we compared the proposed framework with a multi-task learning based segmentation network to jointly estimate the kidney distance maps and classify the kidney pixels. We obtained the results in 20000 iteration numbers. Particularly, the multi-task learning based segmentation network adopted the same network architecture of the kidney boundary distance regression network and included a branch for the kidney pixel classification.

III. EXPERIMENTAL RESULTS

A. Effectiveness of transfer-learning and data-augmentation on the segmentation performance

Fig. 9 shows traces of the training loss and validation accuracy of the kidney boundary detection network trained with 3 different training strategies. These traces demonstrate that the training of the kidney boundary distance regression network converged regardless of the training strategies used. Without the data augmentation, the transfer-learning strategy made the model to better fit the training data and obtained better segmentation accuracy than the random initialization strategy. Although the train loss was relatively larger if the network was trained based on the augmented data, better validation segmentation accuracy was obtained. Validation segmentation accuracy measures of different training strategies are summarized in Table I and example segmentation results are illustrated in Fig. 10, further demonstrating that the transfer learning and data augmentation strategies could make the boundary detection network to achieve better results. The results were obtained at 9000, 1000, 16000 iteration numbers respectively with the different training strategies according to their validation accuracy traces.

TABLE I
SEGMENTATION PERFORMANCE OF DIFFERENT TRAINING STRATEGIES ON THE VALIDATION DATASET

Method	random+noaug	finetune+noaug	finetune+aug
Dice	0.8458 \pm 0.1714	0.9338 \pm 0.0377	0.9421 \pm 0.0343
MD	6.1173 \pm 4.7427	3.2896 \pm 2.0465	3.0804 \pm 2.7781

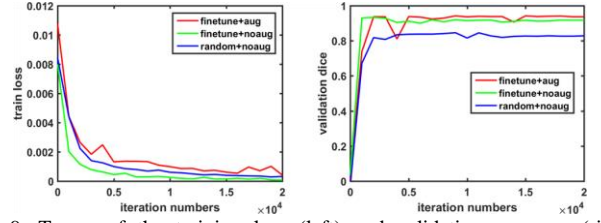


Fig. 9. Traces of the training loss (left) and validation accuracy (right) associated with 3 different training strategies.

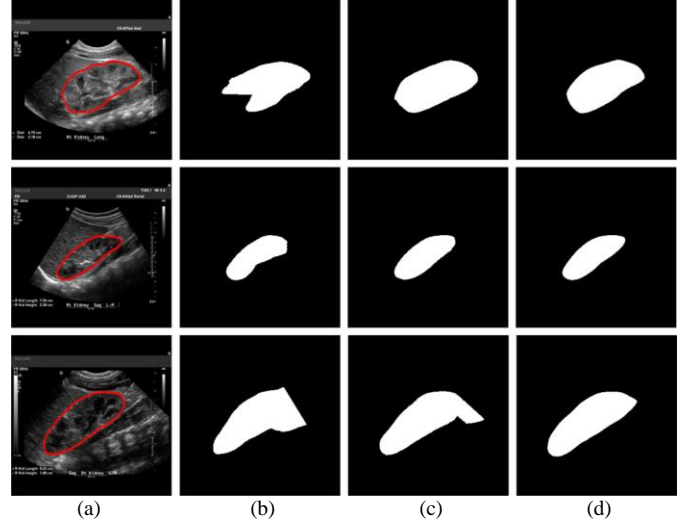


Fig. 10. Example segmentation results obtained with 3 training strategies. (a) input image and ground truth boundary, (b) results of the training from scratch without data augmentation, (c) results of the transfer learning without data augmentation, and (d) results of the transfer-learning with data augmentation.

B. Performance of the kidney boundary detection networks trained using different loss functions

Fig.11 shows example kidney boundaries and masks obtained by the boundary detection networks trained with different distance maps in the validation dataset. Particularly, the kidney masks were closer to the ground truth when the distance maps were normalized with $\lambda = 1$ than other values. When $\lambda = 0.01$, the detected boundaries were much border than the ground truth, while when $\lambda \geq 10$ or $\lambda = 0.1$, the detected boundaries missed some pixels. Such a problem could be overcome to some extent by the post-processing steps, including morphological operations and minimum spanning tree. As summarized in Table II, the kidney segmentation results obtained with $\lambda = 0.1$ and $\lambda = 1$ were comparable, better than those obtained with other parameters. It is worth noting that predicted boundary distance regression results shown in Fig. 11 were not binary maps when $\lambda = 1$ or 10. We set $\lambda = 1$ in all following experiments. We also found that the softmax cross-entropy loss function based pixelwise classification network classified all the pixels into background due to the unbalanced samples.

TABLE II
SEGMENTATION RESULTS OF THE BOUNDARY DETECTION NETWORK TRAINED WITH DISTANCE FUNCTIONS WITH DIFFERENT SETTINGS ON THE VALIDATION DATASET

	$\lambda = 0.01$	$\lambda = 0.1$	$\lambda = 1$	$\lambda \geq 10$
Dice	0.9003 \pm 0.0978	0.9364 \pm 0.0501	0.9421 \pm 0.0343	0.9264 \pm 0.0593
MD	4.2726 \pm 3.4268	2.8683 \pm 1.9569	3.0804 \pm 2.7781	3.3180 \pm 2.7279

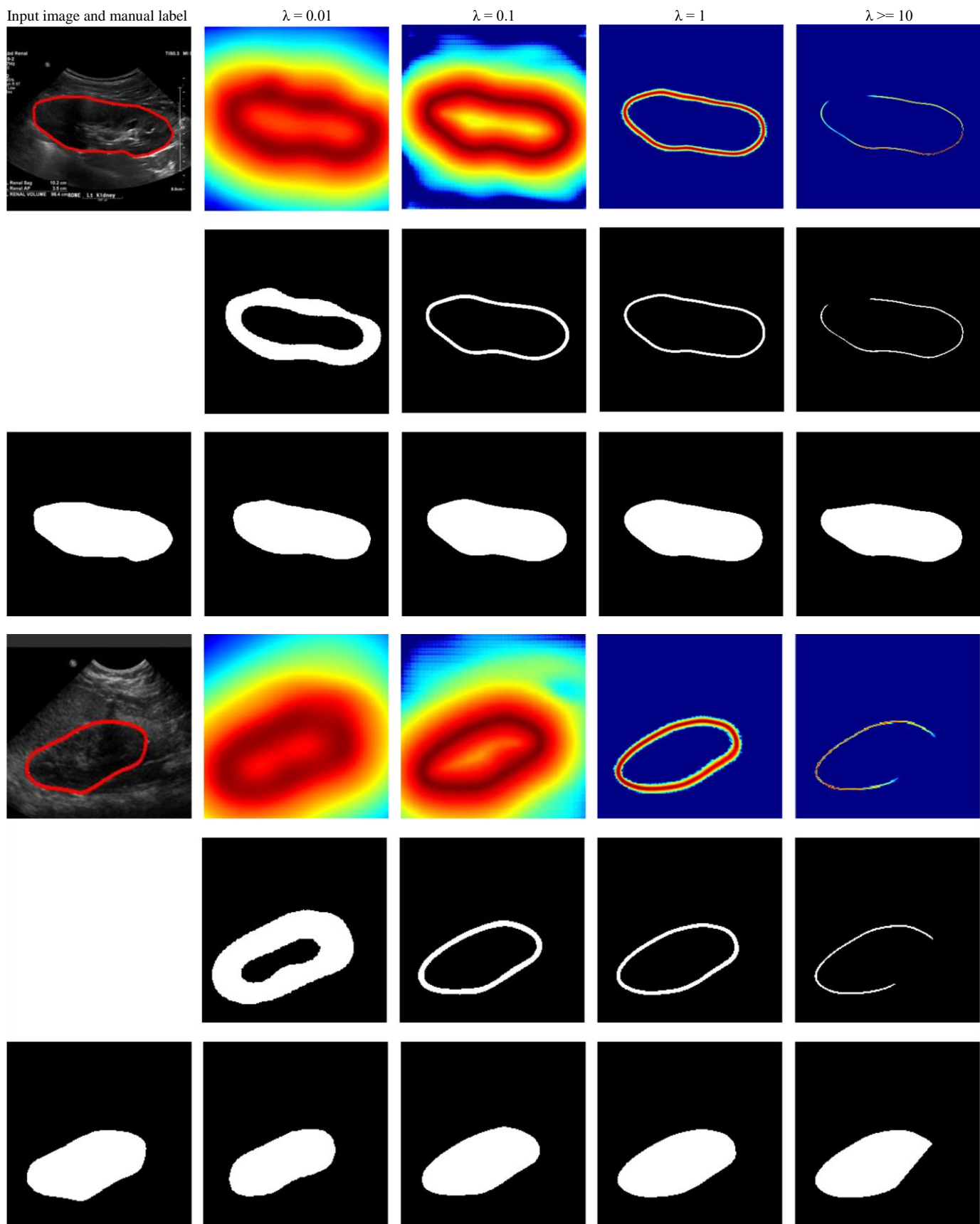


Fig. 11. Results of the kidney boundary detection networks trained using different loss functions. The 1st and 4th rows show predicted boundary distance maps, the 2nd and 5th rows show boundary binary maps, and the 3rd and 6th rows show kidney masks obtained by the morphology operation and minimum spanning tree based post-processing method.

C. Segmentation performance of kidney boundary detection and pixel classification networks

Table III and Table IV show kidney segmentation results of the testing data obtained by the FCNN, Deeplab, and the boundary detection network, trained without the data augmentation or with the data augmentation. The morphology operation and minimum spanning tree based post-processing method was used to obtain kidney masks from the boundary detection network. The results demonstrate that the boundary detection network had significantly better performance than the alternative deep learning segmentation networks that were trained to classify pixels into kidney and non-kidney pixels. The results also demonstrated that the data-augmentation could improve the performance of all the methods under comparison. Fig. 12 shows representative segmentation results obtained by the deep learning methods under comparison with or without the data augmentation. These results demonstrate that our method had robust performance regardless of the variance of kidney shape and appearance. However, FCNN and Deeplab had worse performance for the kidney shown on the 3rd row.

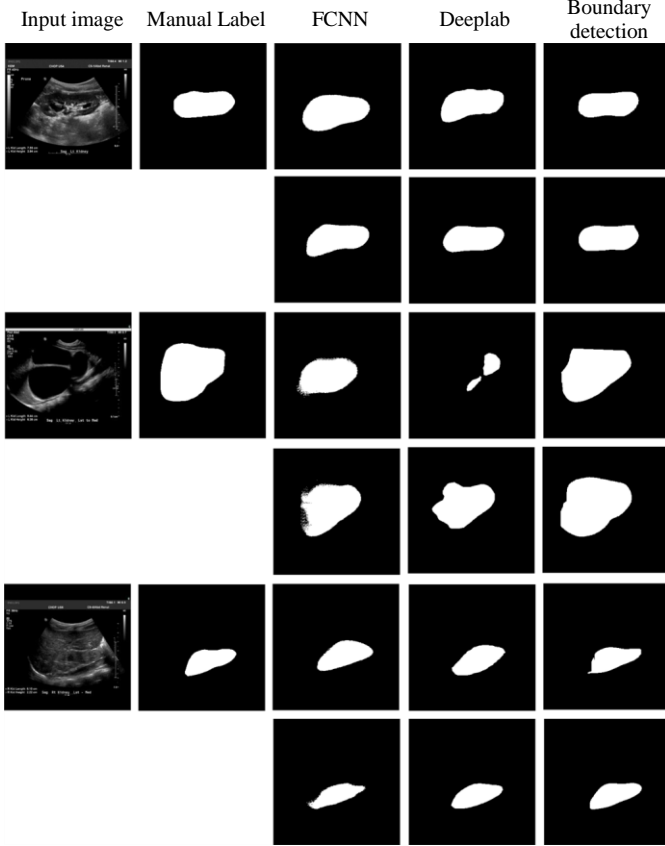


Fig. 12. Representative segmentation results obtained by different deep learning networks trained without data augmentation (the 1st, 3rd, and 5th rows) and with data augmentation (the 2th, 4th, and 6th rows).

D. Comparison of the end-to-end subsequent segmentation network, the boundary detection network, and the multi-task learning based segmentation network

Table V shows segmentation performance of the kidney boundary detection network and the end-to-end subsequent boundary distance regression and pixelwise classification

networks, demonstrating that the end-to-end learning could obtain better performance, although the difference was not statistically significant. Fig. 13 indicated that the proposed framework could improve the boundary detection segmentation results with blurring boundaries. More importantly, we can get the kidney masks from their distance maps without any post-processing step. A further comparison of computational time costs of two solutions indicated that the end-to-end learning was 20 times faster than the morphology and minimum spanning tree based post-processing.

We also combined the proposed boundary distance regression network and the Deeplab mask segmentation network in a multi-task learning framework. In the multi-task learning framework, we set the weight parameter of the two networks to 1. The dice coefficient of segmentation results obtained by the boundary detection task was $90.93\% \pm 4.89\%$ and the dice coefficient of segmentation results obtained by the mask segmentation task was $92.01\% \pm 4.52\%$. We found that accuracy of the mask segmentation network was improved in the multi-task learning framework. However, we also found that the accuracy of the boundary detection network was reduced, partially due to the inaccurate results of the mask segmentation networks.

TABLE V
COMPARISON RESULTS FOR THE PROPOSED MODEL WITH ONLY DISTANCE LOSS FUNCTION AND END-TO-END SUBSEQUENT SEGMENTATION FRAMEWORK ON THE TESTING DATASET.

	Boundary detection network	End-to-end learning
Dice (Mean \pm std)	0.9382 ± 0.0434	0.9430 ± 0.0326
MD (Mean \pm std)	2.8717 ± 2.0665	2.5246 ± 1.4603
Time (sec)	3.75	0.18

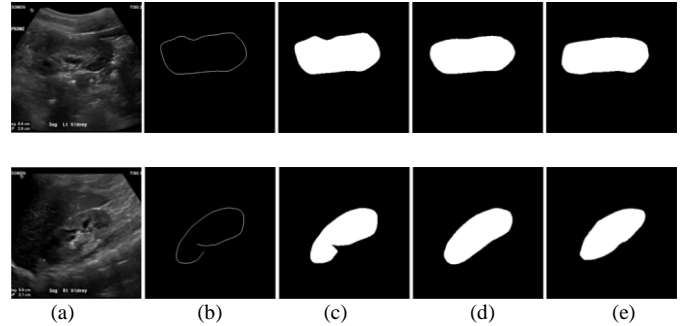


Fig. 13. Results for the boundary detection network and the end-to-end learning networks. (a) input kidney US images, (b) binary skeleton maps of the predicted distance maps, (c) kidney masks obtained with the minimum spanning tree based post-processing, (d) kidney masks obtained by the end-to-end subsequent segmentation network, and (e) kidney masks obtained by manual labels.

IV. DISCUSSIONS AND CONCLUSIONS

In this study, we propose a novel boundary distance regression network architecture to achieve fully-automatic kidney segmentation, and the boundary distance regression network is integrated with a subsequent pixelwise classification network to achieve improved kidney segmentation performance in an end-to-end learning fashion. Our method has been applied to segmentation of clinical kidney US images with large variability in both appearance and shape, yielding promising performance, significantly better than the alternatives under

TABLE III
COMPARISON RESULTS FOR THE PROPOSED METHOD AND OTHER METHODS WITHOUT DATA AUGMENTATION ON THE TESTING DATASET.

	Dice coefficient		Mean distance		Jaccard		Sensitivity		Precision		ASSD	
	Mean \pm std	p-value	Mean \pm std	p-value	Mean \pm std	p-value	Mean \pm std	p-value	Mean \pm std	p-value	Mean \pm std	p-value
FCNN	0.7720 \pm 0.1143	2.8e-11	10.1139 \pm 5.0865	3.5e-11	0.6409 \pm 0.1350	2.3e-11	0.7852 \pm 0.1539	1.6e-09	0.7998 \pm 0.1379	1.7e-10	10.4531 \pm 5.8036	2.3e-11
Deeplab	0.8626 \pm 0.0833	1.3e-09	5.8513 \pm 3.3718	4.9e-08	0.7667 \pm 0.1152	9.9e-10	0.8481 \pm 0.1277	7.0e-07	0.8987 \pm 0.0851	5.0e-04	6.0675 \pm 4.1220	2.4e-09
Proposed	0.9225 \pm 0.0726	-	3.4631 \pm 2.3714	-	0.8625 \pm 0.0972	-	0.9186 \pm 0.0963	-	0.9370 \pm 0.0633	-	3.3570 \pm 2.0938	-

TABLE IV
COMPARISON RESULTS FOR THE PROPOSED METHOD AND OTHER METHODS WITH DATA AUGMENTATION ON THE TESTING DATASET.

	Dice coefficient		Mean distance		Jaccard		Sensitivity		Precision		ASSD	
	Mean \pm std	p-value	Mean \pm std	p-value	Mean \pm std	p-value	Mean \pm std	p-value	Mean \pm Std	p-value	Mean \pm std	p-value
FCNN	0.9038 \pm 0.0626	1.1e-07	4.4814 \pm 3.1166	1.6e-06	0.8298 \pm 0.0951	7.1e-08	0.8980 \pm 0.0953	2.5e-04	0.9217 \pm 0.0787	2.3e-3	4.3511 \pm 2.8988	4.1e-07
Deeplab	0.9149 \pm 0.0456	3.1e-07	3.7902 \pm 2.1976	2.1e-06	0.8635 \pm 0.0734	2.3e-07	0.9108 \pm 0.0659	2.1e-05	0.9261 \pm 0.0688	3.2e-3	3.8021 \pm 2.1307	3.2e-07
Proposed	0.9369 \pm 0.0462	-	2.8717 \pm 2.0665	-	0.8844 \pm 0.0733	-	0.9354 \pm 0.0625	-	0.9437 \pm 0.0599	-	2.8655 \pm 1.9373	-

comparison. Our results have demonstrated that the boundary detection strategy worked better than standard pixelwise classification techniques for segmenting clinical US images with heterogenous appearance. Our results have also demonstrated that the kidney shape registration based data-augmentation method could improve the segmentation performance of the deep learning based methods.

The network initialization is very important for the deep learning based kidney image segmentation. We do not show the U-net network segmentation results because the U-net network failed to converge in our experiment, probably due to that the random initialization method of the U-net network did not work for the kidney US images. In fact, the FCNN and Deeplab networks failed to converge too with the same random initialization method as used in the U-net network. In contrast, the boundary distance regression network successfully converged with the same random initialization. These results might indicate that for the segmentation of clinical kidney US images with varied shapes and appearances the boundary distance regression is a better strategy than the pixel classification strategy.

On the other hand, we also compared the training of the boundary distance regression network from scratch and based on the transfer learning with data augmentation. Although we did not observe substantially improved segmentation accuracy, we found that transfer learning could accelerate the network training converge.

Instead of adopting random transformations to generate more US kidney images, we propose an image registration method to augment the training image data so that the augmented imaging data have meaningful realistic kidney shapes. The results shown in section III C have demonstrated that the data-augmentation method could improve all the deep learning based segmentation methods under comparison in terms of the segmentation accuracy.

The benefits of the end-to-end learning for the kidney segmentation are twofold. First, the end-to-end learning could improve the computational efficiency due to the usage of GPUs. Second, the segmentation performance could be further

improved, as indicated by the results shown in Table V and Fig. 13. We found that the improvement was significant for kidney images with blurry boundaries, although the average performance difference was not statistically significant.

The segmentation results of the multi-task learning network with integrated boundary distance regression network and Deeplab based pixelwise classification network indicated that the boundary distance regression network could improve the performance of the pixelwise classification network. However, a better strategy might be needed to further improve its performance.

Though our kidney segmentation network is built on the pre-trained VGG16 network, our model is not limited to the VGG network. Within the same framework, we could also adopt other semantic segmentation networks with good performance in natural images segmentation tasks, such as ResNet [43] or network built on VGG19 [34], which may further improve the performance of the kidney segmentation results.

REFERENCES

- [1] C. A. Ozmen, *et al.*, "Ultrasound as a diagnostic tool to differentiate acute from chronic renal failure," *Clinical nephrology*, vol. 74, pp. 46-52, 2010.
- [2] J. E. Pulido, *et al.*, "Renal parenchymal area and risk of ESRD in boys with posterior urethral valves," *Clinical journal of the American Society of Nephrology : CJASN*, vol. 9, pp. 499-505, 2014.
- [3] H. Y.-H. Lin, *et al.*, "Association of Renal Elasticity and Renal Function Progression in Patients with Chronic Kidney Disease Evaluated by Real-Time Ultrasound Elastography," *Scientific Reports*, vol. 7, p. 43303, 2017.
- [4] M. Meola, *et al.*, "Imaging in Chronic Kidney Disease," *Contrib Nephrol*, vol. 188, pp. 69-80, 2016.
- [5] Q. Zheng, *et al.*, "Transfer learning for diagnosis of congenital abnormalities of the kidney and urinary tract in children based on ultrasound imaging data," presented at the 2018 IEEE 15th International Symposium on Biomedical Imaging (ISBI 2018), 2018.
- [6] Q. Zheng, *et al.*, "Computer aided diagnosis of congenital abnormalities of the kidney and urinary tract in children based on ultrasound imaging data by integrating texture image features and deep transfer learning image features," *Journal of Pediatric Urology*, 2018.
- [7] H. R. Torres, *et al.*, "Kidney segmentation in ultrasound, magnetic resonance and computed tomography images: A

- systematic review," *Computer Methods and Programs in Biomedicine*, vol. 157, pp. 49-67, 2018.
- [8] R. Ardon, *et al.*, "Fast kidney detection and segmentation with learned kernel convolution and model deformation in 3D ultrasound images," presented at the 2015 IEEE 12th International Symposium on Biomedical Imaging (ISBI), 2015.
 - [9] X. Jun, *et al.*, "Segmentation of kidney from ultrasound images based on texture and shape priors," *IEEE Transactions on Medical Imaging*, vol. 24, pp. 45-57, 2005.
 - [10] Q. Zheng, *et al.*, "A Dynamic Graph Cuts Method with Integrated Multiple Feature Maps for Segmenting Kidneys in 2D Ultrasound Images," *Academic Radiology*, vol. 25, pp. 1136-1145, 2018.
 - [11] J. J. Cerrolaza, *et al.*, "Renal Segmentation From 3D Ultrasound via Fuzzy Appearance Models and Patient-Specific Alpha Shapes," *IEEE Transactions on Medical Imaging*, vol. 35, pp. 2393-2402, 2016.
 - [12] J. J. Cerrolaza, *et al.*, "Segmentation of kidney in 3D-ultrasound images using Gabor-based appearance models," presented at the 2014 IEEE 11th International Symposium on Biomedical Imaging (ISBI), 2014.
 - [13] M. Martín-Fernández and C. Alberola-López, "An approach for contour detection of human kidneys from ultrasound images using Markov random fields and active contours," *Medical Image Analysis*, vol. 9, pp. 1-23, 2005.
 - [14] C. S. Mendoza, *et al.*, "Automatic Analysis of Pediatric Renal Ultrasound Using Shape, Anatomical and Image Acquisition Priors," presented at the Medical Image Computing and Computer-Assisted Intervention – MICCAI 2013, Berlin, Heidelberg, 2013.
 - [15] K. Sharma, *et al.*, "Semi-Automatic Segmentation of Autosomal Dominant Polycystic Kidneys using Random Forests," *arXiv preprint arXiv:1510.06915*, 2015.
 - [16] J. Long, *et al.*, "Fully convolutional networks for semantic segmentation," presented at the Proceedings of the IEEE conference on computer vision and pattern recognition, 2015.
 - [17] L. Chen, *et al.*, "DeepLab: Semantic Image Segmentation with Deep Convolutional Nets, Atrous Convolution, and Fully Connected CRFs," *IEEE Transactions on Pattern Analysis and Machine Intelligence*, vol. 40, pp. 834-848, 2018.
 - [18] X. Zhao, *et al.*, "A deep learning model integrating FCNNs and CRFs for brain tumor segmentation," *Medical image analysis*, vol. 43, pp. 98-111, 2018.
 - [19] O. Ronneberger, *et al.*, "U-net: Convolutional networks for biomedical image segmentation," presented at the International Conference on Medical image computing and computer-assisted intervention, 2015.
 - [20] X. Zhao, *et al.*, "3D Brain Tumor Segmentation Through Integrating Multiple 2D FCNNs," presented at the Brainlesion: Glioma, Multiple Sclerosis, Stroke and Traumatic Brain Injuries, Cham, 2018.
 - [21] P. Jackson, *et al.*, "Deep learning renal segmentation for Fully automated radiation Dose estimation in Unsealed source Therapy," *Frontiers in oncology*, vol. 8, 2018.
 - [22] H. Ravishankar, *et al.*, "Joint deep learning of foreground, background and shape for robust contextual segmentation," presented at the International Conference on Information Processing in Medical Imaging, 2017.
 - [23] H. Ravishankar, *et al.*, "Learning and incorporating shape models for semantic segmentation," presented at the International Conference on Medical Image Computing and Computer-Assisted Intervention, 2017.
 - [24] K. Sharma, *et al.*, "Automatic segmentation of kidneys using deep learning for total kidney volume quantification in autosomal dominant polycystic kidney disease," *Scientific reports*, vol. 7, p. 2049, 2017.
 - [25] J. A. Noble and D. Boukerroui, "Ultrasound image segmentation: a survey," *IEEE Transactions on medical imaging*, vol. 25, pp. 987-1010, 2006.
 - [26] G. Bertasius, *et al.*, "High-for-low and low-for-high: Efficient boundary detection from deep object features and its applications to high-level vision," presented at the Proceedings of the IEEE International Conference on Computer Vision, 2015.
 - [27] L.-C. Chen, *et al.*, "Semantic image segmentation with task-specific edge detection using cnns and a discriminatively trained domain transform," presented at the Proceedings of the IEEE Conference on Computer Vision and Pattern Recognition, 2016.
 - [28] H. Chen, *et al.*, "DCAN: Deep contour-aware networks for object instance segmentation from histology images," *Medical image analysis*, vol. 36, pp. 135-146, 2017.
 - [29] C. Tan, *et al.*, "Deep multi-task and task-specific feature learning network for robust shape preserved organ segmentation," presented at the Biomedical Imaging (ISBI 2018), 2018 IEEE 15th International Symposium on, 2018.
 - [30] H. Tang, *et al.*, "Integrating Deformable Modeling with 3D Deep Neural Network Segmentation," in *Deep Learning in Medical Image Analysis and Multimodal Learning for Clinical Decision Support*, ed: Springer, 2018, pp. 377-384.
 - [31] F. Gokaslan, *et al.*, "Evaluation and outcome of antenatal hydronephrosis: a prospective study," *Ren Fail*, vol. 34, pp. 718-21, 2012.
 - [32] M. Longpre, *et al.*, "Prediction of the outcome of antenatally diagnosed hydronephrosis: a multivariable analysis," *J Pediatr Urol*, vol. 8, pp. 135-9, Apr 2012.
 - [33] A. M. Cheng, *et al.*, "Outcome of isolated antenatal hydronephrosis," *Arch Pediatr Adolesc Med*, vol. 158, pp. 38-40, Jan 2004.
 - [34] K. Simonyan and A. Zisserman, "Very deep convolutional networks for large-scale image recognition," *arXiv preprint arXiv:1409.1556*, 2014.
 - [35] S. Xie and Z. Tu, "Holistically-nested edge detection," presented at the The IEEE International Conference on Computer Vision, 2015.
 - [36] J. B. Kruskal, "On the shortest spanning subtree of a graph and the traveling salesman problem," *Proceedings of the American Mathematical society*, vol. 7, pp. 48-50, 1956.
 - [37] F. L. Bookstein, "Principal warps: thin-plate splines and the decomposition of deformations," *IEEE transactions on pattern analysis and machine intelligence*, vol. 11, pp. 567-585, 1989.
 - [38] S. Boyd and L. Vandenberghe, *Convex optimization*: Cambridge university press, 2004.
 - [39] X. Glorot and Y. Bengio, "Understanding the difficulty of training deep feedforward neural networks," presented at the Proceedings of the thirteenth international conference on artificial intelligence and statistics, 2010.
 - [40] Q. Zheng, *et al.*, "Integrating semi-supervised and supervised learning methods for label fusion in multi-atlas based image segmentation," *Frontiers in Neuroinformatics*, vol. 12, p. 69, 2018.
 - [41] Y. Hao, *et al.*, "Local label learning (LLL) for subcortical structure segmentation: application to hippocampus segmentation," *Hum Brain Mapp*, vol. 35, pp. 2674-97, Jun 2014.
 - [42] R. F. Woolson, "Wilcoxon Signed - Rank Test," *Wiley Encyclopedia of Clinical Trials*, pp. 1-3, 2008.
 - [43] K. He, *et al.*, "Deep residual learning for image recognition," presented at the The IEEE Conference on Computer Vision and Pattern Recognition, 2016.